Mon. Not. R. Astron. Soc. **000**, 000–000 (0000) Printed 1 December 2011 (MN LaTeX style file v2.2)

arXiv:1111.6993v1 [astro-ph.CO] 29 Nov 2011

Elliptical galaxies have been the predominant morphological class for massive galaxies since only $z \sim 1$

Fernando Buitrago[1,2] ⋆, Ignacio Trujillo[3,4], Christopher J. Conselice[1], Boris Häußler[1]

[1] *University of Nottingham, School of Physics & Astronomy, Nottingham, NG7 2RD, U.K.*
[2] *SUPA†, Institute for Astronomy, University of Edinburgh, Royal Observatory, Edinburgh, EH9 3HJ, U.K.*
[3] *Instituto de Astrofísica de Canarias, Vía Láctea s\n, 38200 La Laguna, Tenerife, Spain*
[4] *Departamento de Astrofísica, Universidad de La Laguna, E-38205, La Laguna, Tenerife, Spain*

1 December 2011

ABSTRACT

Present-day massive galaxies are composed mostly of early-type objects. It is unknown whether this was also the case at higher redshifts. In a hierarchical assembling scenario the morphological content of the massive population is expected to change with time from disk-like objects in the early Universe to spheroid-like galaxies at present. In this paper we have probed this theoretical expectation by compiling a large sample of massive ($M_{stellar} \geqslant 10^{11} h_{70}^{-2} M_{\odot}$) galaxies in the redshift interval 0<z<3. Our sample of 1082 objects comprises 207 local galaxies selected from SDSS plus 875 objects observed with the HST belonging to the POWIR/DEEP2 and GNS surveys. 639 of our objects have spectroscopic redshifts. Our morphological classification is done in the V-band restframe both quantitatively (using the Sérsic index as a morphological proxy) and qualitative (by visual inspection). Using both techniques we find an enormous change on the dominant morphological class with cosmic time. The fraction of early-type galaxies among the massive galaxy population has changed from ∼20-30% at z∼3 to ∼70% at z=0. Elliptical galaxies have been the predominant morphological class for massive galaxies since only $z \sim 1$.

Key words: galaxies: evolution – galaxies: high-redshift – galaxies: morphology

1 INTRODUCTION

The present-day massive galaxy population is dominated by objects with early-type morphologies (e.g. Baldry et al. 2004, Conselice et al. 2006). However, it is still unknown whether this was also the case at earlier cosmic epochs. Addressing this question is key to our understanding of the physical processes that drive galaxy evolution, as galaxy morphology is directly linked to the evolutionary paths followed by these objects. In fact, a profound morphological transformation of the massive galaxy population is expected within the currently most favoured galaxy formation scenario, the hierarchical model. For massive galaxies this model predicts a rapid formation phase at 2<z<6 dominated by a dissipational in-situ star formation fed by cold flows (Oser et al. 2010; Dekel et al. 2009; Keres et al. 2005) and/or gas rich mergers (Ricciardelli et al. 2010; Wuyts et al. 2010; Bournaud et al. 2011). At the end of this phase, massive galaxies are expected to be more flattened and disk-like than their lower redshift massive counterparts (Naab et al. 2009). After this monolithic-like formation phase, massive galaxies are predicted to suffer a period of intense bombardment by minor satellites (Khochfar & Silk 2006; Hopkins et al. 2009; Feldmann et al. 2010; Oser et al. 2010) that may eventually transform the original disk-like population into the predominant present-day spheroid-like population.

Although the above scenario is very suggestive of a deep morphological transformation of the massive galaxy population, there is no compelling observational evidence supporting this scenario. However, some recent works suggests that this could be the case (e.g. van der Wel et al. 2011, Cameron et al. 2011, Weinzirl et al. 2011). Probing this transformation is difficult from the observational point of view due to the scarce number of massive galaxies at high-z. However, the advent of wide area and deep near infrared surveys (e.g. Dickinson et al. 2003, Scoville et al. 2007, Conselice et al. 2011) have opened up the possibility of exploring a large number of these galaxies up to high redshifts. In this paper we address, to the best of our knowledge for the first time, the issue of the morphological transformation of massive

---

⋆ E-mail: fernando.buitrago@roe.ac.uk
† Scottish Universities Physics Alliance

galaxies using a statistical representative sample of nearly $\sim$1000 galaxies with $M_\star \geqslant 10^{11} h_{70}^{-2} M_\odot$ obtained from the SDSS DR7 (z$\sim$0; Abazajian et al. 2009), POWIR/DEEP2 (0.2<z<2; Bundy et al. 2006, Conselice et al. 2007) and GNS (1.7<z<3; Conselice et al. 2011) surveys. We have already conducted a morphological quantitative analysis of the above galaxies in previous papers (Trujillo et al. 2007; Buitrago et al. 2008) where we have provided clear evidence for a significant size evolution for these objects since z$\sim$3. However, a visual classification of these galaxies and an analysis of their overall profile shape have been missing. In this paper we take advantage of the combined power of the visual and quantitative morphological analysis to explore how the morphological content of the massive galaxy population has changed with redshift.

The structure of the paper is as follows: Section 2 is devoted to the data description and its analysis, Section 3 presents our main results and in Section 4 we discuss them. At the end of this work we include an Appendix containing the simulations we have performed to test the accuracy of our structural parameter determination in the GNS. On what follows, we adopt a cosmology with Ω_m=0.3, Ω_Λ=0.7 and H$_0$=70 kms^{-1} Mpc^{-1}.

2 DATA

To accomplish our objectives and to be statistically meaningful we need a large number of massive galaxies at all redshifts within our study. Ideally we would also like to study all of our galaxies at a similar restframe wavelength range. This is the reason behind our choice of working with several different surveys. The imaging for the local Universe galaxy reference sample was obtained using the SDSS DR7 (Abazajian et al. 2009) although our sample was selected from the NYU Value-Added Galaxy Catalog (DR6). This catalog includes single Sérsic (1968) profile fits for 2.65×10^6 galaxies (Blanton et al. 2005), from which 1.1×10^6 galaxies have spectroscopic information. Stellar masses come from Blanton & Roweis (2007), which uses a Chabrier (2003) IMF. We limited our work to all the massive ($M_\star \geqslant 10^{11} h_{70}^{-2} M_\odot$) galaxies with spectroscopic redshifts up to $z = 0.03$. We have selected this redshift as an upper limit as it contains a local sample with a number of objects ($\sim$200) similar to the number of galaxies we have in our higher redshift bins. On doing this we assure they are all affected statistically in a similar way. By selecting z=0.03 we also guarantee that these galaxies are retrieved from a sample that is complete in stellar mass. One object in this local sample was rejected as we discovered it was a stellar spike. Our final local sample contains 207 galaxies. We have used the g-band imaging of SDSS to classify visually our local sample.

In the redshift range $0.2 < z < 2$ we utilised the Palomar Observatory Wide-field InfraRed (POWIR)/DEEP2 survey (Bundy et al. 2006, Conselice et al. 2007, 2008). For this part of the analysis, we restricted ourselves to the HST ACS I-band coverage in the Extended Groth Strip (EGS). The sample of massive galaxies selected from this survey constitutes the largest sample of massive galaxies in this redshift range published to date. The EGS field (63 Hubble Space Telescope tiles) was imaged with the Advanced Camera for Surveys (ACS) in the V(F606W, 2660s) and I-band (F814W, 2100s). Each tile was observed in 4 exposures that were combined to produce a pixel scale of 0.03 arcsec with a Point Spread Function (PSF) of 0.12 arcsec Full Width Half Maximum (FWHM). The depth reached is $I_{AB} = 27.52$ (5σ) for point sources, and about 2 magnitudes brighter for extended objects. Complementary photometry in the B, R and I bands was taken with the CFH12K camera at the CFHT 3.6-m telescope and in the K_s and J bands with the WIRC camera at the Palomar 5-m telescope. Standard photometric techniques (see Conselice et al. 2007) were performed in order to get both photometric redshifts and masses (using again Chabrier IMF). In total, 421 massive galaxies posses spectroscopic redshifts out of the total 795 in this survey. There were another 35 massive galaxies in the parent sample, but they were excluded as they are identified as AGN and hence they may skew our results.

For the highest redshift bins we used the GOODS NICMOS Survey[1] (GNS; Conselice et al. 2011). The GNS is a large HST NICMOS-3 camera program of 60 pointings centered around massive galaxies at $z = 1.7 - 3$ at 3 orbits depth, for a total of 180 orbits in the F160W (H) band. Each tile (52"x52", 0.203"/pix) was observed in six exposures that were combined to produce images with a pixel scale of 0.1 arcsec, and a PSF of ~ 0.3 arcsec FWHM. Photometric redshift and stellar masses were derived in a similar way as in POWIR. Some (11) spectroscopic redshifts were added a posteriori to the data (Popesso et al. 2008, Barger et al. 2009). This sample is the largest massive galaxies compendium (80 objects) at $1.7 < z < 3$ we are aware of.

2.1 Quantitative and visual morphological classification

Once we selected the final sample of objects, the surface brightness distributions of all our galaxies were examined using GALFIT (Peng et al. 2010). We fit all our objects with a single Sérsic model convolved with the PSF of the images, selected using real stars. Different, non saturated, stars were used to check the reliability of our quantitative morphological analysis results. The exact details of our analysis can be found in Trujillo et al. (2007; POWIR sample) and Buitrago et al. (2008; GNS sample). In relation to the SDSS imaging, although the NYU catalog already provides structural parameters obtained using Sérsic fits to the galaxies, for the sake of consistency with our methodology, we ran GALFIT on the SDSS images of these galaxies to obtain structural parameters. It is known that the NYU catalog has a systematical underestimation of the Sérsic index, effective radius and total flux, as it is reported in the simulations performed in Blanton et al. (2005) and in the appendix of Guo et al. (2009). Our findings agree with this fact, as we find an offset of $26 \pm 2\%$ for the circularised effective radius values of our galaxies and another $14 \pm 3\%$ for the Sérsic indices.

In addition to the quantitative morphological analysis explained above, visual morphological classifications were derived for all the galaxies in our sample. To assure a high reliability in our results, two authors of this paper (FB and IT, with checks by CC) classified visually all the galaxies in an independent way. We divided our sample according to

---

[1] http://www.nottingham.ac.uk/astronomy/gns/

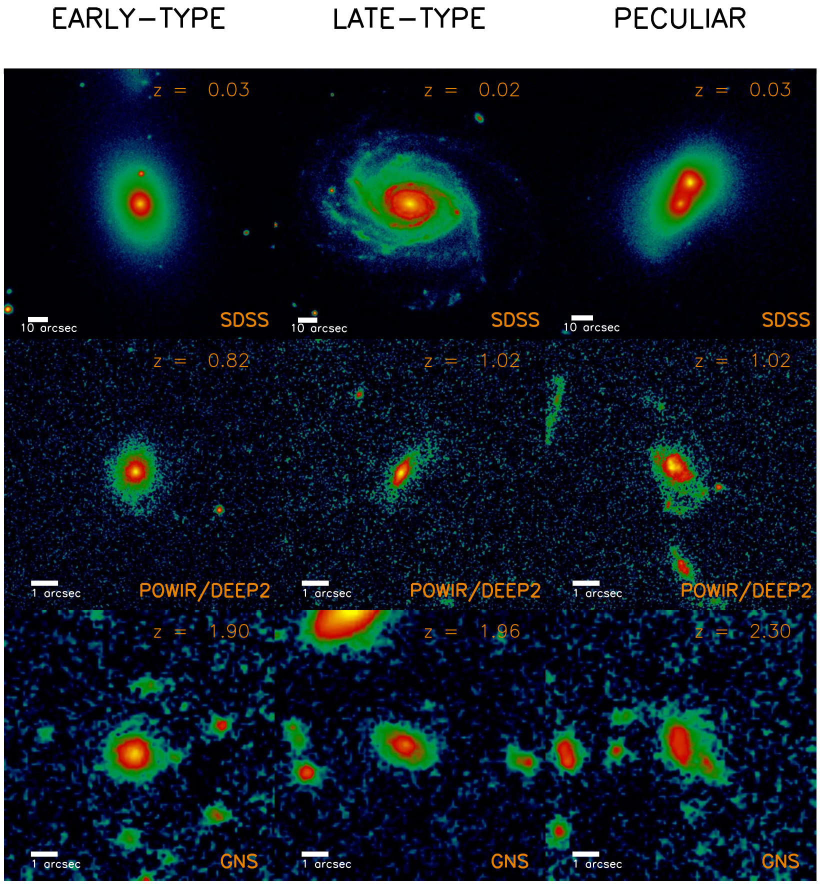

Figure 1. Some examples illustrating our morphological criteria (columns) for different galaxies in our sample. Each row shows galaxies of the different surveys. Please note the different scales of each image due to each galaxy redshift (lower left corner); according to the cosmology used in this work, 10 arcsec in SDSS are ∼ 6 kpc at z∼0.03, while 1 arcsec in the HST imaging at $z \geqslant 1$ is ∼ 8 kpc. Despite the decrease in angular resolution and the cosmological surface brightness dimming with redshift, the exquisite HST depth and resolution (∼10 times better than ground-based SDSS imaging) allow us to explore the morphological nature of the high-z galaxies. Note that irregulars and mergers are in the same morphological class (peculiars).

the Hubble classification scheme into spheroid-like objects (E+S0 or early-type), disk-like objects (S or late-type) and peculiar galaxies (either irregular galaxies or ongoing mergers). In Figure 1 we show some examples of our classification scheme at different redshifts. Very conspicuous bulge systems were identified as early-type objects. Both E and S0 galaxies are hence included together in the same morphological class. We avoid segregating between E and S0 since, at high-z, it is a difficult task to distinguish between these two types of galaxies, and we prefer to remove this potential source of error. Spiral or late-type morphologies are detected by a central brightness condensation located at the centre of a thin disk containing more or less visible spiral arms of enhanced luminosity. Lastly we joined irregular (unsymmetrical) galaxies and mergers in the same class, again to avoid any missclassification at high-z where the differences between these types are more difficult to interpret.

It is not straightforward to asses the robustness of our visual classifications as this is a pattern recognition problem and as such cannot be addressed by standard algorithm procedures. Nevertheless, at z∼0, we can compare our results with other alternatives coming from independent studies. First, we compare our results with the SDSS Bayesian automated morphological classification by Huertas-Company et al. (2011). There are 190 out of our 207 galaxies in common where can make a direct comparison. They applied support vector machine techniques (Huertas-Company et al. 2008) to associate a probability to each galaxy being E, S0, Sab or Scd. For those galaxies where they have assigned a probability larger than 90% of pertaining to a given class, their neural network agrees with our visual classification for 89% of the early-types and 68% of the late-types. Moreover, all our SDSS local galaxies have been visually classified within the Galaxy Zoo project (Lintott et al. 2011). We find that 112 out of the 121 galaxies that we classified as early-type are classified as ellipticals by Galaxy Zoo (i.e. ∼93%). For spiral galaxies we get 48 out of 62 (i.e. ∼77%). The discrepancies in our late-type galaxies identifications arise from the difficulty to interpret S0 galaxies without the astronomer's "trained-eye" intervention and, as stated previously, they are included as early-type objects throughout our study. Consequently, our local classification seems to be robust.

2.2 Potential observational biases

We acknowledge, however, that at higher redshifts visual morphological classification is more controversial for several reasons. First, the cosmological surface brightness dimming may affect the recognition of fainter galactic features and second, the angular resolution is poorer at higher redshift. Nonetheless, the first effect is compensated by the increase of the intrinsic surface brightness (e.g. Marchesini et al. 2007; Prescott, Baldry & James 2009, Cirasuolo et al. 2010) of the galaxies due to having a higher star formation rate in the past, and the fact that their stellar populations are younger. In relation to the angular resolution, at z=0.03, one arcsec is equivalent to ∼0.6 kpc, whereas at 1<z<3 it is ∼8.0 kpc. Fortunatelly, the higher resolution imaging used for exploring the morphologies of our high-z galaxies (FHWM∼0.1-0.3 arcsec) compared to the local ones (FWHM∼1.0-1.5 arcsec) alleviates this problem, although in general, a smoother surface brightness distribution due to the worse resolution is expected. All these effects combined imply that at higher redshifts there would be a larger number of featureless objects that visually would be confused with early-type galaxies. We will show in the next section that this is the opposite of what we find, ultimately giving stronger support to the results of this paper.

2.3 Morphological K-corrections

The K-correction effect is another potential source of error both within the quantitative and visual morphological classification. We have selected our filters at each survey to minimise this effect, and to observe the galaxies as close as possible to the g-band restframe. Nonetheless, our classification at $1.3 \lesssim z \lesssim 2$ could be compromised by using F814W as this filter is tracing the UV restframe of our targets.

We explored how relevant this effect is by analysing the properties of 24 galaxies with z<2 in our POWIR/DEEP2 sample which also have H-band NICMOS imaging. In Trujillo et al. (2007) we discussed the size difference between the optical and near-infrared for these galaxies (their Fig. 4). We found a non-systematic bias, but a scatter of 32% for these measurements of the effective radius. With regards to the Sérsic index, we found an offset of 30±9% towards larger indices in the H-band. The difference in the visual morphology between the I and the H-bands shows that 19 galaxies (79±8%) have the same morphology in the two filters, while only 5 (21 ± 8%) are catalogued differently. Our errors for visual classifications are the binomial standard deviations. We found in ACS 13 (54 ± 10%) early-type galaxies (10 in NICMOS, 42 ± 10%), 6 (25 ± 9%) late-type galaxies (10 in NICMOS, 42 ± 10%) and 5 (21 ± 8%) peculiar galaxies (4 in NICMOS, 17 ± 8%).

In addition to this analysis of galaxies in the EGS, we compared the difference between the I and H band morphologies for those galaxies in the GNS with 1.7<z<2 (which is the redshift interval where our POWIR/DEEP2 and GNS sample overlap). We used the I-band ACS imaging of the GOODS fields (Giavalisco et al. 2004). Postage stamp images for 20 common galaxies were retrieved from the RAINBOW database (Barro et al. 2011). Our GALFIT analysis showed that the effective radius and the Sérsic index are recovered without any significant offset, but with a large scatter as in the aforementioned Trujillo et al. (2007). Regarding their visual morphologies, we found that 6 galaxies (30 ± 10%) were not possible to classify reliably due to the few pixels that compose their image, most probably due to dust obscuration (Buitrago et al. 2008, Bauer et al. 2011). For the remaining 14 galaxies, 11 (55 ± 11%) have the same visual morphology, while for 3 galaxies (15 ± 8%) there is a difference. For the detections in the ACS camera, 4 (28 ± 12%) are early-types (6 for their NICMOS counterparts, 43 ± 11), 6 (43 ± 11%) are late-types (5 in NICMOS, 36 ± 13%) and 4 (28 ± 12%) are peculiars (3 in NICMOS, 21 ± 11%). Summarising, K-correction undoubtedly play a role, but visual morphologies are robust against these changes within our study.

2.4 Axis ratios

Finally, a further test we can conduct to quantify the robustness of our visual classification is to explore the axis ratio distribution of our objects. The axis ratio distribution of local disk galaxies has a mean value of ∼0.5 (Ryden 2004). On the other hand, the axis ratio distribution of the nearby E/S0 population is known to peak at around 0.7-0.8 (Ryden, Forbes & Terlevich et al. 2001). Figure 2 displays the distributions of axis ratios in our sample according to our visual morphological determinations. In Table 1 we also show the mean axis ratio for our different galaxy population as a function of redshift. We find that the objects that are visually classified as early-type galaxies have a typical axis ratio of ∼0.7 (independent of their redshift). Also, for galaxies visually classified as disks, the axis ratio is independent of the redshift with an average b/a∼0.55. Both values are in good agreement with the expectation from the local Universe. This test reinforces the idea that our visual classifications are accurate.

3 RESULTS

The evolution of galaxy morphology with redshift can be addressed in two different ways: quantitative (exploring how their structural parameters have changed with time), and qualitative (probing how the visual appearance has evolved with redshift). In the local Universe, the structural properties of massive galaxies (mainly its light concentration) can be linked with their appearance. In particular, as a first approximation one can identify disk or late-type galaxies with those galaxies having lower values of the Sérsic index (n∼1; Freeman 1970) and early-type galaxies with those having a profile resembling a de Vaucouleurs (1949) shape (n∼4). This crude segregation based on the Sérsic index was shown to work reasonably well by Ravindranath et al. (2004). Whether this equivalence also holds at higher redshift is not clear, and in this paper we explore this issue.

Table 1 lists the mean values of the structural parameters from the galaxies in our sample, splitting them among a number of redshift ranges and their visual morphologies. Concerning effective radius measurements, we retrieve again the reported size decrease for massive galaxies with redshift. As explained in Section 2.4, axis ratios values per morphological class are independent of redshift, which agree with our morphological classifications. Finally, there is a tendency

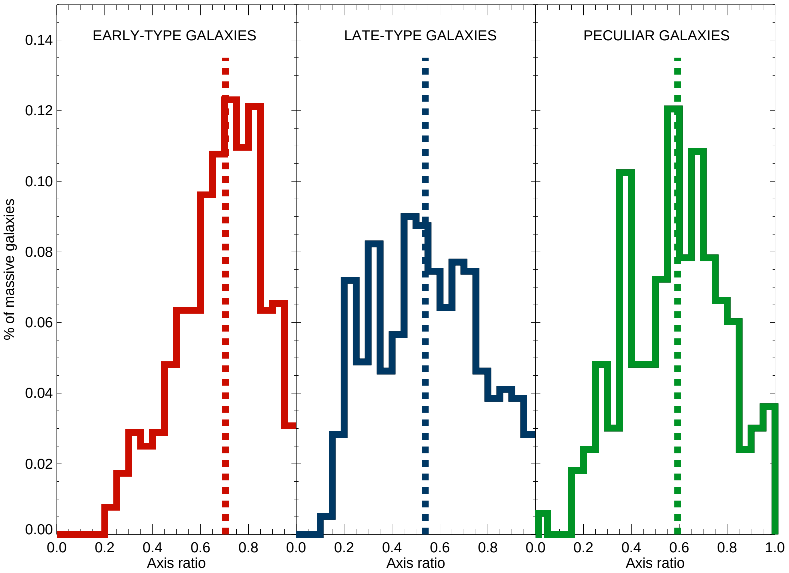

Figure 2. Axis ratio distributions for our sample of massive galaxies according to their visual morphology. Vertical dashed lines are the median values of each histogram (0.70, 0.54 and 0.59, respectively). While for disks the distribution is rather symmetrical, this is not the case for early-type objects, which peak at higher axis ratio values. Van der Wel et al. (2011) argued that massive galaxies with axis ratios $\lesssim$ 0.5 are most probably related with late-type objects, as this histograms confirm. Interacting/peculiar galaxies should be taken out of these considerations. The histograms are also in agreement with the estimations of axis ratio distributions for local early-type and late-type objects (Ryden, Forbes & Terlevich et al. 2001; Ryden 2004). This fact highlight the reliability of our visual morphological classification.

for the Sérsic indices (observed using both mean and median values, see Fig. 3) to become progressively smaller at increasingly higher redshifts. Moreover, there is a separation in the average Sersic index for late and early-type massive galaxies at all redshifts.

In Fig. 4, we show the Sérsic index distribution for our different visually classified morphological types as a function of redshift. At all redshifts, massive galaxies identified visually as late-types show low Sérsic index values. This reinforces the idea that the stellar mass density distributions of rotationally supported systems are close to an exponential profile. However, the distribution of the Sérsic index for these late-type galaxies show a tail towards larger values. This is normally interpreted as the result of the bulge component. In fact, the excess of light caused by the bulge at the centre of the disk will increase the value of this concentration parameter when the galaxies are fitted just using a single Sérsic model. Interestingly, we observe that at higher redshift the prominence of this tail of higher Sérsic indices decreases for the late-type galaxies.

One could be tempted to interpret this result as a consequence of the disappearance of prominent bulges at higher redshifts. However, a detailed exploration of this issue is beyond the scope of this paper. In the same figure, we show the distribution of the Sérsic index for massive galaxies visually classified as early-types. We see that at low redshift, the distribution of Sérsic indices for these galaxies predominantly show large values of concentration as it is expected. Up to z∼1.5 there is a peak around n∼4-6 (see also Table 1). A general trend is also observed: there is a progressive shift towards lower and lower Sérsic index values as redshift increases.

We conducted a series of Kolmogorov-Smirnov (KS) tests in order to check the significance of the changes in the Sérsic index with redshift. In Figure 7 we show the evolution of the KS significance levels for the different morphological types in our sample of massive galaxies. The KS test is a non-parametric method of comparing probability distributions. We used as a base comparison the lowest redshift bin Sérsic index distribution (left panel), and at the highest redshift one (right panel). Despite the uncertainties, mainly due to the number statistics, it seems that the distributions of Sérsic indices gradually change from low to high redshift, and vice-versa. When we conduct the analysis using the high-z bin as the reference instead of the local one, the evolution of the Sérsic index distribution is statistically more significant on average. The fact that several redshift bins repeat significance level values in the left panel shows us the Sérsic index distributions of early types are similar to the one at low-z, while this is not true for late-types. Possible explanations are the homology of early-type galaxies, and the double-peak which only exists in our local late-types Sérsic indices, that is linked with the growth in the light profile wings. Consequently, the checks we carried out attempting to characterise the change of Sersic indices with redshift are positive (namely the Table 1, the Figure 3 and these KS tests), even though the KS comparison with the local Sérsic index distribution is not as smooth as the others. The reason for this change or shift we observe could be either a real effect, produced by a decrease in the tail of the surface brightness distribution of the massive galaxies

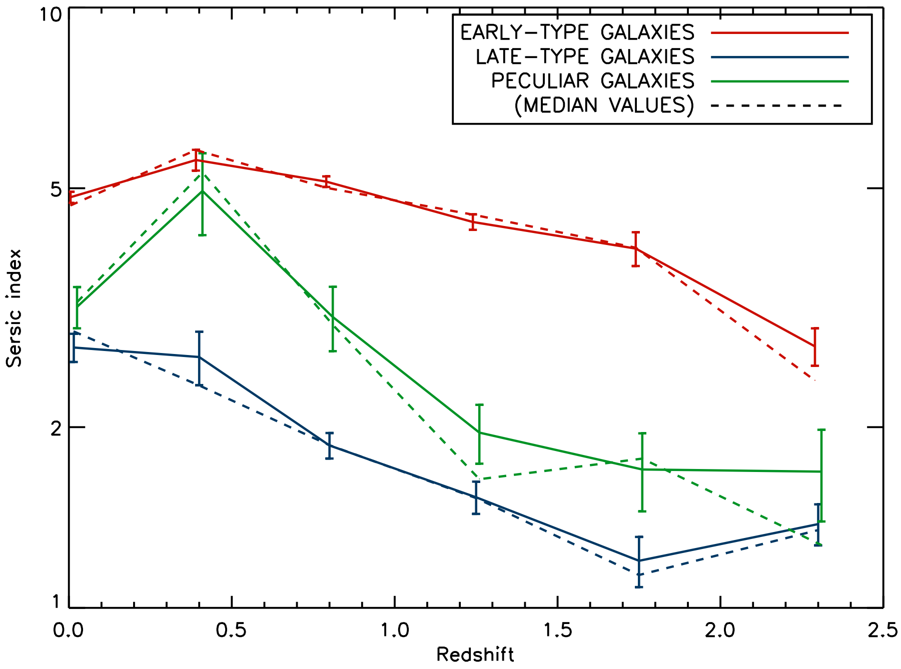

Figure 3. Evolution of the mean Sérsic index values over redshift according the visual classifications of the galaxies within our sample (see also Table 1). Data points for early-types and peculiars are slightly offset for the sake of clarity. Dashed lines are similar but taking median values instead. Errors bars are the uncertainty of the mean ($\sigma/\sqrt{(N-1)}$, being σ the standard deviation and N the total number of galaxies for each point). They are slightly larger at 0.2<z<0.6 because of the comparatively poor statistics at this redshift interval. From that epoch to higher redshifts there is a clear separation between early-type massive galaxies and the rest of visual types, being all the average Sérsic indices lower at increasing redshift.

at higher redshift, or an artificial one, produced by a bias at recovering large Sérsic index values.

To explore this last possibility we have conducted extensive simulations to check whether there is any bias in the recovery of the Sérsic index. In the case of the POWIR sample the simulations are fully explained in Trujillo et al. (2007). In this study we did not find any significant trend in either the sizes or the concentration of the galaxies (see their Fig. 3), except for a slight understimation of $\sim 20\%$ in the Sérsic index of the very faint $I_{AB} > 24$ spheroid-like galaxies. We carried out a similar analysis here for the galaxies in the GNS sample.

The results of these simulations are comprehensively explained in the Appendix A at the end of this work. In summary we find that for objects with disk-like surface brightness profiles (i.e n_{input}<2.5), both sizes and Sérsic indices are recovered with basically no bias down to our limiting explored H-band magnitude. However, by increasing the input Sérsic index we find biases in the determination of the sizes and n. For a galaxy with n_{input}~4 and H=22.5 mag (our typical magnitude within the GNS catalogue), the output effective radii are $\sim$ 10% smaller and output Sérsic indices are $\sim$ 20% smaller than our input galaxies. The results of these simulations however show that the decrease in the Sérsic index we observe from z~2.5 to z=0 for the spheroid-like population (which is around a factor of ~2) can not be explained fully as a result of the bias on recovering the Sérsic index.

We used the output of our simulations (H_{output}, $r_{e,output}$ and n_{output}) to estimate the intrinsic (input) values of our sample and provide a more accurate representation of the evolution of the Sérsic indices at high-z. On average, the observed Sérsic indices grow by ~10% after these changes, although the individual values per galaxy depend on its exact position in the 3D space defined by the output magnitude, Sérsic index and effective radius. In Figure 4 we implemented these corrections for the GNS, and also for the POWIR/DEEP2 data using Trujillo et al. (2007) simulations. For the sake of clarity, Figure 5 displays the same results but without any corrections in two highest redshift bins. Even after these corrections are applied the trend we observe towards lower Sérsic indices at higher redshifts is maintained. In fact, the corrections are minor. We discuss and interpret the histograms of Fig. 4 in the next section. In relation to the distribution of the Sérsic index for the galaxies we classified as interacting or irregulars, we see a larger spread.

Many studies (e.g. Shen et al. 2003; Barden et al. 2005; McIntosh et al. 2005; Trujillo et al. 2006) have used n=2.5 as a quantitative way to segregate between early and late-type galaxies. We explore, using this criteria, how the percentages of the different types of massive galaxies evolve with redshift. This is shown in Fig. 6a. This figure clearly indicates that the fraction of massive galaxies with lower Sérsic index values has dramatically increased at higher redshift. If the association between the Sérsic index and the global

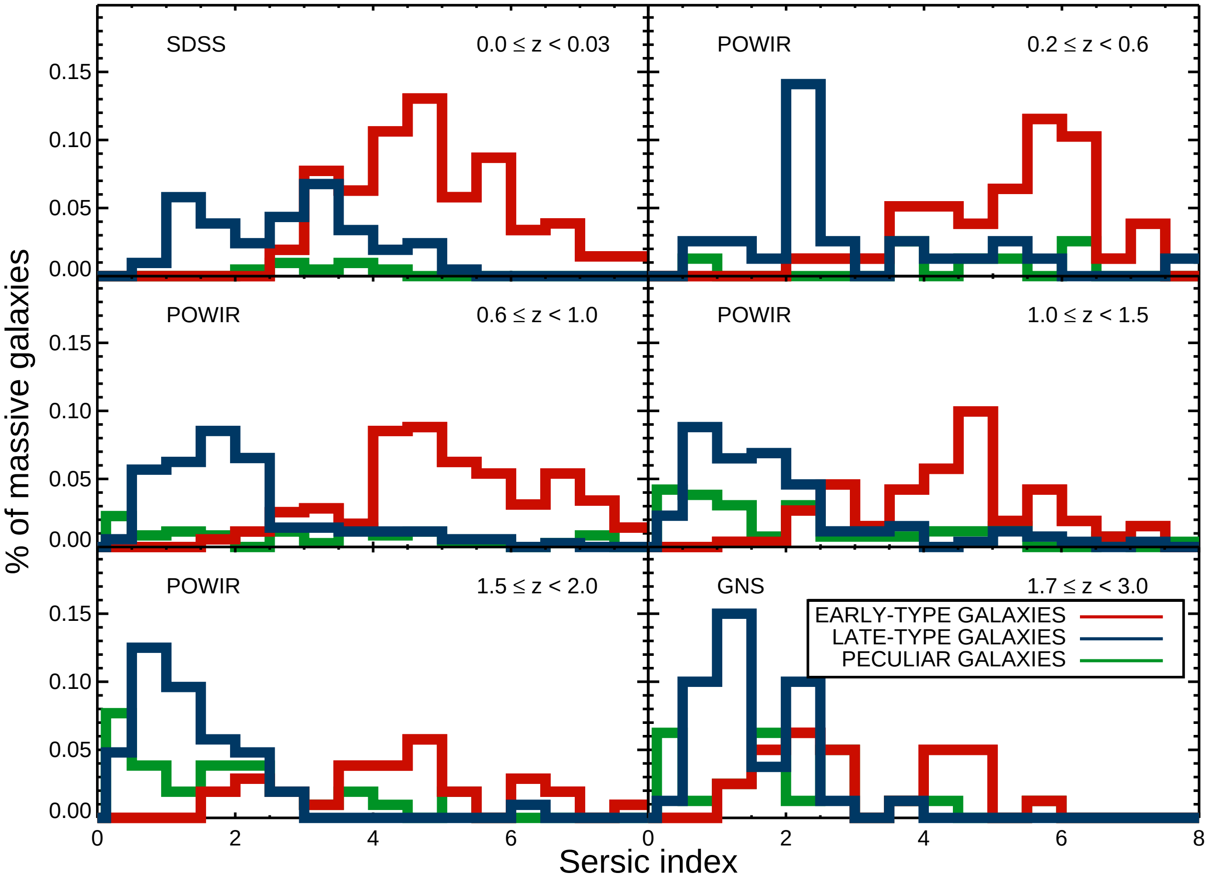

Figure 4. Sérsic index distribution of massive ($M_\star \geqslant 10^{11}h_{70}^{-2}M_\odot$) galaxies at different redshift intervals. The Sérsic indices of the individual galaxies have been corrected following the simulations presented in Trujillo et al. (2007; POWIR) and the Appendix of this paper (GNS). Color coding is related with visual morphology: blue for late-type galaxies, red for early-type galaxies and green for peculiar (irregulars/mergers) galaxies. It is pertinent to note that the sharp peak for late-type objects at 0.2<z<0.6 is due to the small number statitics for this class of massive galaxies at this redshift interval (see Table 1). For our SDSS sample, the Sérsic index of disky objects are mainly located between 1<n<3 but for some galaxies extend up to $n = 5$. Conversely, the Sérsic index of spheroid galaxies starts at n∼3 and then peaks at n∼5. The distributions of the Sérsic index steadily shift to lower values at increasing redshift with the high Sérsic index values progressively disappearing.

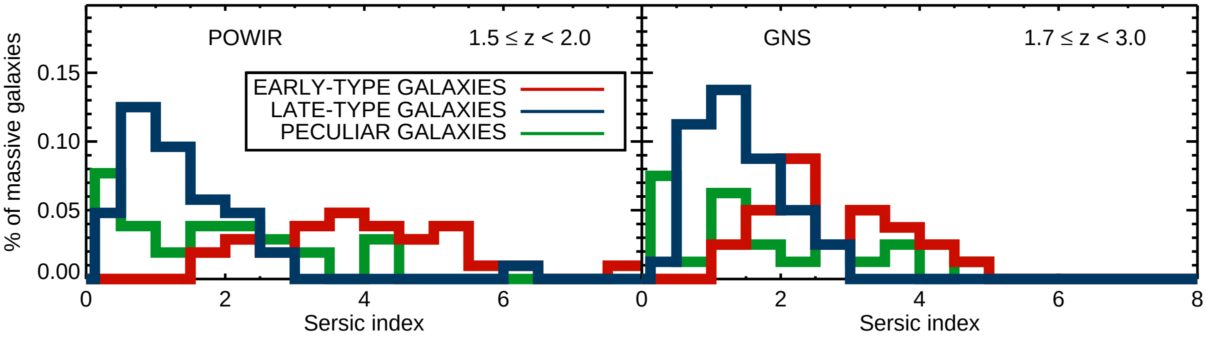

Figure 5. These are the highest redshift histograms of the Figure 4, showing the observed Sérsic indices values, without any a posteriori correction based on Trujillo et al. (2007) or our current GNS simulations (Appendix A). The more noticeable change is seen for the GNS data, where it is very conspicuous the non-existence of any large ($n > 4.62$) Sérsic index. The difference between these histograms and the ones presented in Figure 4 is small.

morphological type that holds at low redshift also applies at high-z this would imply that massive galaxies at the high-z universe were mostly late-type (disk) galaxies. However, there is no guarantee that such an association holds at all redshifts. For this reason, we explore the evolution of the fraction of different galaxy types with redshift using the visual morphologies (see Fig. 6b). We find that the population of visually classified massive disk galaxies remains almost constant with redshift with perhaps a slight (if any) increase. The most dramatic changes are associated with the early-type and irregular/mergers classes. The fraction of visually classified E/S0 galaxies increased by a factor of three since z∼3 to now, whereas a reverse situation is seen for the irregular/merging galaxies. This latter fact agrees with merging becoming more important in massive galaxy evolution at increasing redshift (Conselice et al. 2009, Bluck et al. 2009, 2011). At z∼2.5 late-type and peculiar objects account for the majority of massive galaxies. One of the most important outcome of Fig. 6 is that the E/S0 type has been the dominant morphological fraction of massive galaxies only since z∼1.

The number density of massive galaxies has significantly changed since z∼3 (e.g. Rudnick et al. 2003; Pérez-González et al. 2008, Mortlock et al. 2011, Conselice et al. 2011) with a continuous increase in the number of these objects in the last ∼11 Gyr. In order to probe the emergence of the different galaxy types explored in this paper we have estimated the number density evolution of each class. To do this, we have used the Schechter fits to the stellar mass functions provided by Pérez-González et al. (2008; their Table 2). We have integrated these functions for all massive objects with $M_{stellar} \geqslant 10^{11} h_{70}^{-2} M_{\odot}$. We have later multiplied those numbers by the fractions we have estimated for the different classes of galaxies explored in this work. We show these number density evolution in Fig. 6c & 6d. The number density of both disk-like and spheroid-like massive galaxies, according to their Sérsic index, have changed with time. This evolution is particularly significant for spheroid-like objects which are now a factor of ∼10 more numerous per unit volume than at z∼2. The number of massive disks has also increased as cosmic time progresses, but at a lower rate than spheroid galaxies. Finally, the number density of massive irregular/merging galaxies has grown only very midly, if at all, in the last ∼11 Gyr.

4 DISCUSSION

The evidence collected in the previous section suggests that there is a strong evolution in the morphological properties (both quantitative and qualitative) of the massive galaxy population over time. At high redshift, in agreement with the theoretical expectation, the dominant morphological classes of galaxies are late-types and peculiars. Consequently, the morphological and structural types of the majority of the massive galaxies at a given epoch has dramatically evolved as cosmic time increases. Two effects could play a role towards explaining this significant change of the dominant morphological class. On one hand, the galaxies that are progressively been added into the family of massive objects (i.e. by the merging of less massive galaxies) are incorporated with already spheroidal morphologies. On the other hand, the already old massive galaxies can also evolve towards spheroidal morphologies due to frequent mergers. For instance, frequent minor mergers (López-Sanjuan et al. 2010, Kaviraj 2010, López-Sanjuan et al. 2011, Bluck et al. 2011) with the massive galaxy population will destroy existing stellar disks, and also would be responsible for the appearance of long tails in their luminosity profiles. This scenario could explain why the evolution towards spheroid-like morphologies is stronger when we use the Sérsic index n instead of the visual classification. In fact, the surface brightness of nearby massive ellipticals are well described with large Sérsic indices due to their bright tails or envelopes. These wings, however, seem to disappear at higher and higher redshifts (see Table 1 or Figure 3) just leaving the inner (core) region of the massive galaxies (Bezanzon et al. 2009; Hopkins et al. 2009; van Dokkum et al. 2010; Carrasco, Conselice & Trujillo 2010). The disappearance of these tails is also connected with the dramatic size evolution reported in previous works (see e.g. Trujillo et al. 2007; Buitrago et al. 2008; Trujillo, Ferreras & De la Rosa 2011). Consequently, it is not only that the typical morphology of the massive galaxy population is changing with redshift, but also that there is a progressive build-up of their tails, making the morphological evolution appears more dramatic when we use the Sérsic index instead of the visual classification as a morphological segregator.

If we were just using the information contained in the change of the fraction of morphological types with redshift we would be tempted to explain the morphological evolution as being just a consequence of a transformation from one class to another, however, the evolution in the number density of all the classes suggests a more complex scenario. In fact, one of the results we can conclude from the evolution of the number densities of all the massive galaxy classes is that high-z massive disk-like galaxies can not be the only progenitors of present-day massive spheroid-like galaxies. They are just simply not enough in number to explain the large increase of the number density of elliptical galaxies at low redshifts.

All the morphological classes, with the maybe exception of irregular/merging galaxies, have increased their number densities with cosmic time. These irregular/merging galaxies also have shorter structural life-spans than the other types, and therefore the galaxies in this class must be replenished through time. This emergence of massive galaxies is more efficient (by a factor ∼2) at creating spheroid-like galaxies than disk-like objects from z∼1 to now (see Fig. 6). The reason why the formation of elliptical galaxies is more efficient at recent times than it was in the past is possibly linked to the less availability of gas during mergers creating new galaxies (Khochfar & Silk 2006, 2009, Shankar et al. 2010, Eliche-Moral et al. 2010), and thus more likely to contain denser and more concentrated light profiles (Bluck et al. 2011).

5 SUMMARY

Using a large compilation of massive ($M \geqslant 10^{11} h_{70}^{-2} M_{\odot}$) galaxies (∼1100 objects) since z∼3 we have addressed the issue of the morphological change of this population with time. We have found that there is a profound transformation

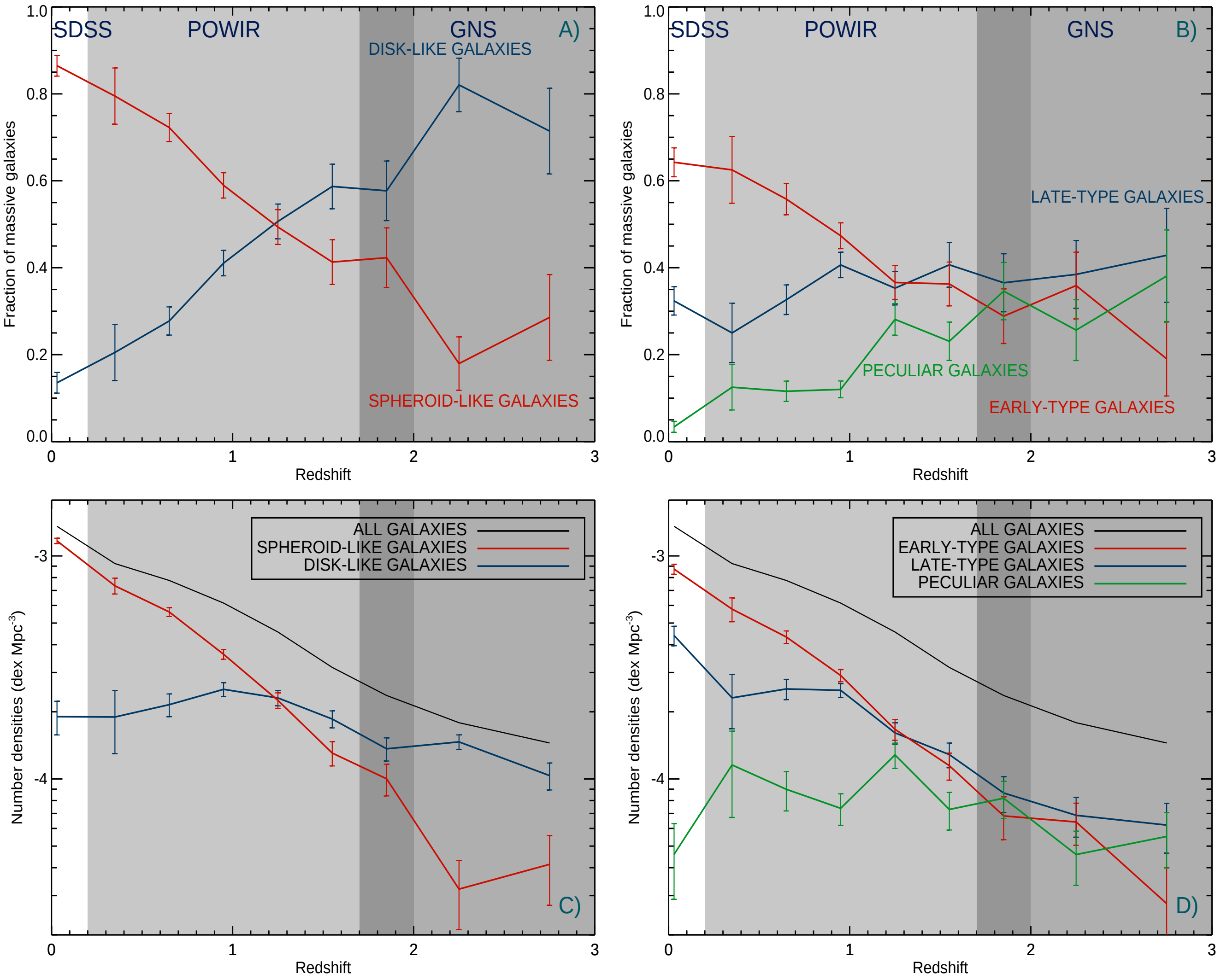

Figure 6. Panel A): Fraction of massive ($M_* \geqslant 10^{11} h_{70}^{-2} M_\odot$) galaxies showing disk-like surface brightness profiles ($n < 2.5$) and spheroid-like ones ($n > 2.5$) as a function of redshift. Different color backgrounds indicate the redshift range expanded for each survey: SDSS, POWIR/DEEP2 and GNS. Error bars are estimated following a binomial distribution. Sérsic indices are corrected based on our simulations (Trujillo et al. 2007 and Appendix A in the present paper). B): Same as Panel A) but segregating the massive galaxies according to their visual morphological classification. Blue color represents late type (S) objects and red early type (E+S0) galaxies, while peculiar (ongoing mergers and irregulars) galaxies are tagged in green. Panel C): Number density evolution of massive galaxies splitted depending on the Sérsic index value. The solid black line corresponds to the sum of the different components. Panel D): Same as panel C) but segregating the massive galaxies according to their visual morphological type.

in the morphological content of massive galaxies during this cosmic interval. Massive galaxies were typically disk-like in shape at z $\gtrsim$ 1 and elliptical galaxies have been only the predominant massive class since that epoch. The fraction of early-type morphologies in massive galaxies has changed from ~20-30% at z~3 to ~70% at z=0.

We have addressed the morphological transformation of the massive galaxies using a quantitative approach, based on GALFIT fits to the surface brightness distribution of the galaxies, and a qualitative approach based on visual classifications. Both analysis agree on a clear morphological change in the dominant morphological class with time. In particular, the quantitative approach, which uses the Sérsic index as a morphological segregator, shows that the number of galaxies with low Sérsic index at high-z was higher than in the present day universe. We interpret this as a consequence of two phenomena: a decrease in the number of early-type galaxies at higher redshift plus an intrinsic decrease of the Sérsic index values of those elliptical galaxies at earlier cosmic times due to the lost of their extended envelopes.

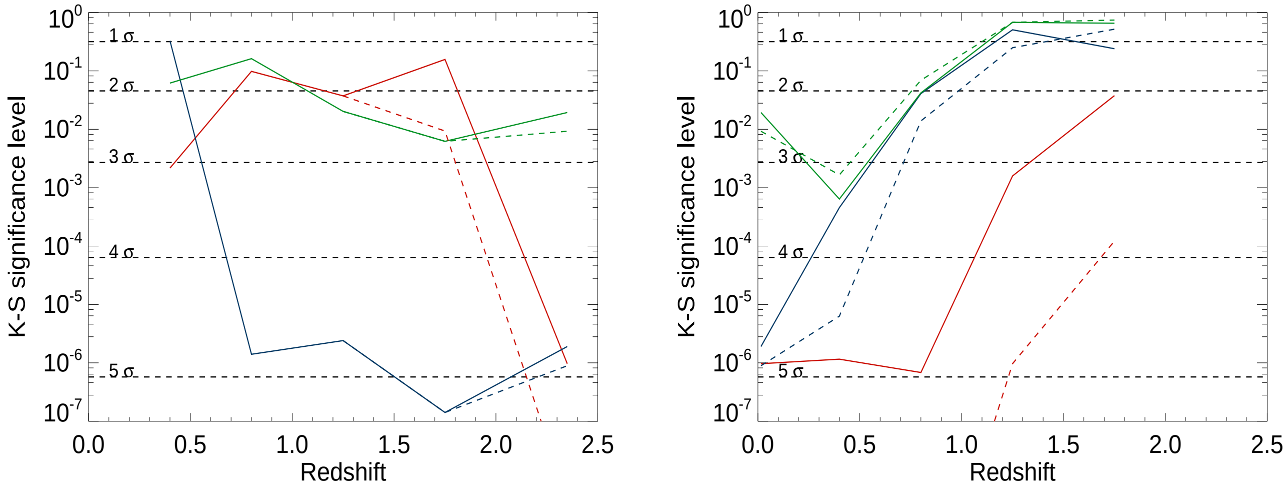

Figure 7. Kolmogorov-Smirnov significance levels comparing the SDSS local sample Sérsic index distribution with all the other redshift bins (left panel) and the GNS highest redshift bin Sérsic index distribution against the rest of the distributions (right panel). The color coding is the same as in the previous figures: red is for early-type galaxies, blue is for late-type galaxies and green is for peculiar galaxies. Dashed lines represent the same results but taking into account the corrections for Sérsic indices inferred from our simulations. The reason why dashed lines encompass the whole plot in the right panel is that the last distribution (GNS) is available with and without corrections, but this does not occur for the local SDSS sample. The general trends show that, within our uncertainties, the distributions are diverging from the local relation (left panel) or progressively converging up to the highest redshift bin (right panel). The distributions with the Sérsic indices corrected according to our simulations show a lower departure with respect to the fiducial distribution, but still a significant one.

6 ACKNOWLEDGEMENTS

This paper would have not been possible without hospitality of the IAC, in particular that of IT and Jesús Falcón-Barroso. We acknowledge the help of Jesús Varela on finding the necessary information of the SDSS sample, Judit Bakos for assistance with SDSS imaging and sky substraction and also Juan E. Betancort, Sylvain de la Torre and Inés Flores-Cacho for their scientific feedback, apart from the contributions from the GNS team. We gratefully thank Steven Bamford, Nathan Bourne, Carlos López-Sanjuan and Pablo Pérez-González for useful discussions. This work has been supported by the STFC, NASA through NASA/STScI grant HST-GO11082, the Leverhulme Trust, and the Programa Nacional de Astronomía y Astrofísica of the Spanish Ministry of Science and Innovation under grant AYA2010-21322-C03-02.

REFERENCES

Abazajian K. N. et al. 2009, ApJS, 182, 543
Abraham et al. 2007, ApJ, 675, 234
Baldry I. K. et al. 2004, ApJ, 600, 681
Barden M. et al. 2005, ApJ, 635, 959
Barger, A. J., Cowie L. L. & Wang W.-H. 2008, ApJ, 689, 687
Barro G. et al. 2011, ApJS, 193, 13
Bauer A. E. et al. 2011, MNRAS, 417, 289
Bertin E. & Arnouts S., 1996, A&AS, 117, 393
Bezanson R. et al., ApJ, 697, 1290
Blanton M. R. et al. 2005, ApJ, 629, 143
Blanton M: R. & Roweis S. 2007, AJ, 133, 734
Bluck A. F. L., Conselice C. J., Bouwens R. J., Daddi E., Dickinson M., Papovich C., Haojing Y., 2009, MNRAS, 394, l51
Bluck A. F. L. et al. 2011, ApJ submitted & arXiv:1111.5662
Bournaud F. et al. 2011, ApJ, 730, 4
Buitrago F. et al. 2008, ApJ, 687, L61
Bundy K. et al., 2006, ApJ, 651, 120
Cameron E. et al. 2011, ApJ submitted & arXiv:1007.2422
Carrasco E. R., Conselice C. J. & Trujillo I. 2010, MNRAS, 405, 2253
Cassata P. et al. 2010, ApJ, 714, L79
Cassata P. et al. 2011, ApJ submitted & arXiv: 1106.4308
Cava A. et al. 2010, MNRAS, 409, L19
Ceverino D. et al. 2010, MNRAS, 404, 2151
Chabrier G., 2003, PASP, 115, 763
Cimatti A. et al. 2008, A&A, 482, 21
Cirasuolo M., McLure R. J., Dunlop J. S., Almaini O., Foucaud S., Simpson C., 2010, MNRAS, 401, 1166
Conselice C. J., 2006, ApJ, 639, 120
Conselice C. J. et al., 2007, MNRAS, 381, 962
Conselice C. J., Bundy K., U V., Eisenhardt P., Lotz J., Newman, J., 2008, MNRAS, 383, 1366
Conselice C. J., Yang C., Bluck A. F. L., 2009, MNRAS, 394, 1956
Conselice C. J. et al. 2011a, MNRAS, 413, 80

Table 1. Observed mean structural parameters (± the standard deviations) for visually classified massive ($M_\star > 10^{11} h_{70}^{-2} M_\odot$) galaxies at 0<z<3

Early-type galaxies

Redshift Range	Number of galaxies	Survey	Effective radius (kpc)	Sérsic index	Axis ratio (b/a)	Mean stellar mass ($10^{11} h_{70}^{-2} M_\odot$)
0-0.03	133	SDSS	7.15 ± 1.56	4.83 ± 1.19	0.74 ± 0.13	1.26 ± 0.22
0.2-0.6	44	POWIR	4.77 ± 2.05	5.57 ± 1.46	0.71 ± 0.15	1.51 ± 0.45
0.6-1.0	184	POWIR	3.52 ± 1.79	5.13 ± 1.41	0.67 ± 0.19	1.78 ± 0.69
1.0-1.5	104	POWIR	2.06 ± 1.04	4.39 ± 1.32	0.63 ± 0.19	1.70 ± 0.51
1.5-2.0	30	POWIR	1.31 ± 0.73	3.97 ± 1.38	0.65 ± 0.17	1.56 ± 0.37
1.7-3.0	25	GNS	1.30 ± 0.55	2.73 ± 0.96	0.68 ± 0.11	1.58 ± 0.42

Late-type galaxies

Redshift Range	Number of galaxies	Survey	Effective radius (kpc)	Sérsic index	Axis ratio (b/a)	Mean stellar mass ($10^{11} h_{70}^{-2} M_\odot$)
0-0.03	67	SDSS	8.44 ± 3.28	2.71 ± 1.19	0.60 ± 0.22	1.21 ± 0.14
0.2-0.6	26	POWIR	5.39 ± 1.77	2.62 ± 1.28	0.50 ± 0.25	1.40 ± 0.30
0.6-1.0	124	POWIR	4.91 ± 2.04	1.86 ± 0.98	0.54 ± 0.21	1.53 ± 0.49
1.0-1.5	95	POWIR	4.81 ± 1.90	1.53 ± 0.87	0.57 ± 0.23	1.58 ± 0.41
1.5-2.0	42	POWIR	3.88 ± 1.51	1.20 ± 0.73	0.50 ± 0.20	1.61 ± 0.49
1.7-3.0	34	GNS	2.55 ± 1.18	1.38 ± 0.62	0.54 ± 0.18	1.55 ± 0.50

Peculiar galaxies

Redshift Range	Number of galaxies	Survey	Effective radius (kpc)	Sérsic index	Axis ratio (b/a)	Mean stellar mass ($10^{11} h_{70}^{-2} M_\odot$)
0-0.03	7	SDSS	8.39 ± 2.22	3.17 ± 0.61	0.72 ± 0.13	1.16 ± 0.13
0.2-0.6	8	POWIR	4.93 ± 2.26	4.95 ± 2.04	0.56 ± 0.23	1.16 ± 0.08
0.6-1.0	42	POWIR	4.16 ± 2.39	3.05 ± 2.40	0.56 ± 0.20	1.65 ± 0.49
1.0-1.5	58	POWIR	3.83 ± 1.64	1.96 ± 1.62	0.61 ± 0.18	1.65 ± 0.51
1.5-2.0	30	POWIR	2.53 ± 1.68	1.70 ± 1.36	0.53 ± 0.26	1.81 ± 0.68
1.7-3.0	21	GNS	2.45 ± 1.04	1.69 ± 1.31	0.61 ± 0.18	1.44 ± 0.34

Daddi, E., et al. 2005, ApJ, 626, 680
Damjanov I., et al. 2009, ApJ, 695, 101
Dekel A. et al. 2009, Nature, 457, 451
de Vaucouleurs G., 1948, AnAp, 11, 247
Dickinson M. et al. 2003, The Mass of Galaxies at Low and High Redshift: Proceedings of the European Southern Observatory, pp. 324
Eliche-Moral M. C. et al. 2010, A&A, 519, 55
Feldmann R., Carollo C. M., Mayer L. 2011, ApJ, 736, 88
Freeman K.C.1970, ApJ, 160, 811
Giavalisco M., et al., 2004, ApJ, 600, L93
Häußler et al. 2007, ApJS, 172, 615
Hopkins P. F., Bundy K., Murray N., Quataert E., Lauer T. R., Ma C.-P., 2009, MNRAS, 398, 898
Huertas-Company M., Rouan D., Tasca L., Soucail G., Le Fèvre, O., 2008, A&A,, 478, 971
Huertas-Company, M. et al. 2011, A&A, 525, 157
Kaviraj, S. 2010, MNRAS, 406, 382
Kereš D., Katz N., Weinberg D. H., Davé R., 2005, MNRAS, 363, 2
Khochfar S. & Silk J. 2006, ApJ, 648, L21
Khochfar S. & Silk J. 2009, MNRAS, 397, 506
Kriek et al. 2008, ApJ, 677, 219
Lintott, C. et al. 2011, MNRAS, 410, 166
López-Sanjuan C. et al. 2010, A&A, 518, 20
López-Sanjuan C. et al. 2011, A&A, 530, 20
Marchesini D. et al. 2007, ApJ, 656, 42
Marleau, F. R., & Simard, L. 1998, ApJ, 507, 585
McIntosh D. et al., 2005, ApJ, 632, 191
Mortlock A. et al. 2011, MNRAS, 413, 2845
Naab T., Johansson P. H., Ostriker J. P., ApJ, 2009, 699, L178
Oser L. et al. 2010, ApJ, 725, 2312
Peng C. Y. et al. 2010, AJ, 139, 2097
Pérez-González P. G., et al., 2008, ApJ, 675, 234
Prescott M., Baldry, Ivan K., James P. A., 2009, MNRAS, 397, 90
Popesso P. et al., 2009, A&A, 494, 443
Ravindranath S. et al. 2004, ApJ, 604, L9
Ricciardelli E. et al. 2010, MNRAS, 406, 230
Rudnick G. et al. 2003, ApJ, 599, 847
Ryden B. S., Forbes D. A. & Terlevich A. I. 2001, MNRAS, 326, 1141
Ryden B. S. 2004, ApJ, 601, 214

Sérsic J.-L., 1968, Atlas de Galaxias Australes (Córdoba: Observatorio Astronómico)
Shankar F. et al. 2011, arXiv: 1105.6043
Shen S. et al., 2003, MNRAS, 343, 978
Trujillo I., Förster Schreiber N. M., Rudnick G., et al., 2006a, ApJ, 650, 18
Trujillo I., Conselice C. J., Bundy K., Cooper M. C., Eisenhardt P., Ellis R., 2007, MNRAS, 382, 109
Trujillo I., Ferreras I. & De la Rosa I., 2011, MNRAS, 415, 3903
Viero M. et al. 2010, MNRAS submitted & arXiv:1008.4359
van der Wel A. et al. 2011, ApJ, 730, 38
van Dokkum P. G. et al. 2010, ApJ, 709, 1018
Weinzirl T. et al. 2011, ApJ accepted & arXiv:1107.2591
Wuyts S. et al. 2010, ApJ, 722, 1666

APPENDIX A: GOODS NICMOS SURVEY MASSIVE GALAXIES SIMULATIONS

The purpose of this Appendix is to explore the robustness of the structural parameters of the massive galaxies (1.7<z<3) in our GNS sample (H-band, F160W filter, HST NICMOS-3 camera, 3 orbits depth; Conselice et al. 2011). As explained in the main text of the paper, a set of simulations similar to the ones presented here were already conducted for the ACS imaging used to analyze the galaxies in the redshift interval 0.2<z<2 (Trujillo et al. 2007). To identity the ranges of the structural parameters to explore in our simulations, we use as a guide the ranges found in the quantitative morphological analysis based on GALFIT of the real GNS massive galaxies (Buitrago et al. 2008). These were:

$$0.15 < r_e(arcsec) < 0.61$$

$$0.34 < n < 4.62$$

$$0.19 < ar < 0.92$$

$$-84.03 < pa < 85.28$$

$$20.5 < H_{AB}(mag) < 24$$

where r_e, n, ar, pa, H_{AB} stand for effective radius, Sérsic index, axis ratio, position angle and derived H_{AB}-band magnitude. The only exceptions were one galaxy with $n = 0.17$ and two others with $24 < H_{AB} < 24.5$. Taking these quantities into account, we simulated 16000 galaxies utilising the IDL routines built for Häußler et al. (2007), with the structural parameters randomized within these ranges:

$$0.15 < r_e(arcsec) < 2.0$$

$$0.25 < n < 8.0$$

$$0.1 < ar < 1.0$$

$$-89.99 < pa < 90.0$$

$$20 < H_{AB}(mag) < 25$$

The structural parameters of the mock galaxies were distributed linearly along the full parameter space, except for the effective radii which were logarithmically sampled as we specially wanted to explore objects with small angular radii due to the observed compactness of massive galaxies at high-z.

Images of every mock galaxy were created placing these objects randomly in the GNS pointings. We placed a mock galaxy on each GNS poiting for every simulation in order to avoid altering the typical density (i.e. number of neighbour galaxies) of the GNS imaging. Each model galaxy (i.e. the 2D surface brightness distribution following the Sérsic function) was convolved with a representative PSF. Specifically we used one of the five natural stars which were utilised in Buitrago et al. (2008). To obtain errors in the same way as in that paper, we also ran GALFIT using these five different stars and then taking the mean values.

We have identified that the main source of uncertainty in the NICMOS data is the change of the PSF among the different pointings. To illustrate how this affects the recovery of the structural parameters we first present in Figure 8 and 9 how our parameters are recovered when we use the same PSF for creating and recovering the mock galaxies. In Figure 10 and 11, we show the effects on the parameters when we compare the input values with the average values obtained using the five different PSFs.

In Figure 10 we show the relationship between the relative errors in the structural parameters (magnitude, effective radius and Sérsic index) versus the galaxy input magnitude. The relative errors are calculated as *(output-input)/input* (i. e., a negative % refer to cases where the output is smaller than the input and vice-versa). The left column of the plot displays the structural parameters of individual mock galaxies, whereas the right column shows their means in bins of 0.5 mag. The mean values of the structural parameters were derived using a robust method which removes the 5σ outliers. Error bars represent the standard deviation of the sample. To appreciate how the effect on the structural parameter is linked to the input Sérsic index of the mock galaxies we split the sample into four groups ($0 < n < 2$, $2 < n < 4$, $4 < n < 6$ and $6 < n < 8$). The results shown in Fig. 10 are tabulated in the Table 4. At increasing Sérsic index values, the recovery of the structural parameters is more affected. We note that galaxies with low Sérsic index are well recovered down to our faintest magnitude. An average galaxy in our GNS sample (H=22.5 mag) with an input Sérsic index of n=4 will have its effective radius biased only by a ∼15% and its Sérsic index around $\lesssim$ 25%.

In addition to the dependence of the apparent magnitude of the objects on recovering their structural parameters, in Figure 11 we explore what is the effect of the size (lower row) and intrinsic shape (upper row) for this matter. Galaxies are colour coded in these figures according to their magnitude. Combining the information contained in Fig. 10 and 11, we find that the key parameters for retrieving accurate structural parameters are the apparent magnitude and the Sérsic index. The effective radius of the objects play a minor role. The results show on Fig. 11 are tabulated in the Table 5.

The most interested output of our tests using the mean value from the fits of different PSFs is that the size of the source plays now a fundamental role at characterising the error on the structural parameters. As expected, large sources are less affected by changes in the PSF and the bias on the structural parameters remain basically the same as when we use just a single PSFs. However, at smaller sizes the effect of not knowing accurately the PSF at the source implies that the Sérsic index uncertainty is large, although sizes are retrieved accurately. Summarising, neither any effect or combination of effects is large enough to modify the main results of this paper. Moreover, as stated on the main text of this paper, we use these simulations to correct, based on the observed (output) apparent magnitude, effective radius and Sérsic index, the structural parameters presented in this work.

Table 2. Relative errors (%) and standard deviations on the structural parameters depending on the apparent magnitude (see Fig. 8).

	$0 < n < 2$	$2 < n < 4$	$4 < n < 6$	$6 < n < 8$
$20.0 < H_{AB,input}(mag) < 20.5$				
$\delta L/L$	0.39 ± 1.75	-0.53 ± 3.21	-1.85 ± 6.24	-2.62 ± 7.36
$\delta r_e/r_e$	0.09 ± 2.03	-1.16 ± 5.27	-4.63 ± 12.35	-7.19 ± 15.54
$\delta n/n$	-0.34 ± 4.08	-3.22 ± 6.20	-6.25 ± 10.59	-7.62 ± 12.07
$20.5 < H_{AB,input}(mag) < 21.0$				
$\delta L/L$	0.21 ± 2.61	-0.99 ± 5.46	-2.95 ± 7.61	-3.43 ± 8.20
$\delta r_e/r_e$	0.01 ± 2.98	-2.33 ± 8.31	-6.78 ± 14.35	-9.16 ± 17.30
$\delta n/n$	-0.97 ± 5.63	-3.51 ± 8.48	-7.69 ± 11.25	-9.13 ± 12.68
$21.0 < H_{AB,input}(mag) < 21.5$				
$\delta L/L$	-0.12 ± 3.85	-1.34 ± 6.93	-2.60 ± 10.14	-3.62 ± 10.74
$\delta r_e/r_e$	-0.40 ± 4.58	-2.81 ± 11.39	-5.08 ± 20.67	-7.85 ± 21.32
$\delta n/n$	-1.42 ± 8.21	-5.65 ± 12.94	-7.72 ± 15.04	-9.08 ± 16.12
$21.5 < H_{AB,input}(mag) < 22.0$				
$\delta L/L$	-0.05 ± 5.17	-2.56 ± 10.93	-3.76 ± 13.39	-4.95 ± 13.55
$\delta r_e/r_e$	-0.50 ± 4.79	-4.98 ± 17.21	-8.46 ± 25.80	-9.54 ± 29.76
$\delta n/n$	-2.47 ± 9.68	-6.85 ± 14.97	-10.83 ± 20.77	-11.80 ± 21.14
$22.0 < H_{AB,input}(mag) < 22.5$				
$\delta L/L$	-1.03 ± 7.28	-2.87 ± 12.06	-5.83 ± 15.87	-6.79 ± 18.50
$\delta r_e/r_e$	-1.70 ± 8.48	-5.33 ± 17.56	-8.22 ± 27.02	-14.28 ± 32.00
$\delta n/n$	-3.55 ± 17.15	-8.50 ± 19.65	-11.86 ± 22.91	-17.65 ± 26.70
$22.5 < H_{AB,input}(mag) < 23.0$				
$\delta L/L$	-1.46 ± 9.27	-3.40 ± 18.16	-6.97 ± 19.19	-11.04 ± 22.58
$\delta r_e/r_e$	-1.48 ± 10.75	-5.55 ± 26.98	-10.61 ± 33.02	-18.60 ± 37.86
$\delta n/n$	-3.74 ± 22.80	-8.20 ± 25.31	-13.99 ± 28.88	-21.90 ± 29.83
$23.0 < H_{AB,input}(mag) < 23.5$				
$\delta L/L$	-2.70 ± 18.92	-5.54 ± 22.91	-10.57 ± 22.24	-14.38 ± 25.00
$\delta r_e/r_e$	-3.38 ± 18.65	-7.10 ± 33.57	-15.11 ± 38.94	-24.55 ± 39.17
$\delta n/n$	-5.29 ± 29.66	-11.14 ± 34.34	-18.92 ± 32.87	-29.79 ± 31.89
$23.5 < H_{AB,input}(mag) < 24.0$				
$\delta L/L$	-1.28 ± 21.90	-8.12 ± 22.41	-11.57 ± 26.88	-17.93 ± 26.23
$\delta r_e/r_e$	-3.81 ± 26.00	-10.21 ± 33.56	-17.86 ± 43.47	-32.17 ± 39.63
$\delta n/n$	0.61 ± 37.18	-18.35 ± 36.38	-24.90 ± 37.94	-35.02 ± 33.59
$24.0 < H_{AB,input}(mag) < 24.5$				
$\delta L/L$	-0.99 ± 28.30	-7.27 ± 34.80	-16.06 ± 33.78	-15.98 ± 34.87
$\delta r_e/r_e$	-2.13 ± 36.39	-13.48 ± 41.48	-29.16 ± 44.22	-32.70 ± 42.43
$\delta n/n$	-7.57 ± 43.98	-27.35 ± 41.82	-39.53 ± 40.77	-44.10 ± 36.75
$24.5 < H_{AB,input}(mag) < 25.0$				
$\delta L/L$	12.20 ± 51.04	2.50 ± 51.58	-5.73 ± 44.09	-15.50 ± 43.68
$\delta r_e/r_e$	-12.85 ± 45.18	-22.74 ± 46.45	-31.77 ± 43.55	-36.15 ± 48.64
$\delta n/n$	-11.73 ± 49.37	-38.99 ± 42.35	-44.67 ± 42.69	-47.58 ± 40.68

Table 3. Relative errors (%) and standard deviations on the structural parameters (see Fig. 9)

$\delta r_e/r_e$	$20 < H_{AB}(mag) < 21.5$	$21.5 < H_{AB}(mag) < 23$	$23 < H_{AB}(mag) < 25$
$0 < n < 2$	-0.04 ± 3.09	-1.00 ± 7.97	-4.89 ± 31.91
$2 < n < 4$	-2.14 ± 8.27	-5.13 ± 20.61	-12.66 ± 38.79
$4 < n < 6$	-5.71 ± 15.87	-9.08 ± 28.73	-22.12 ± 42.84
$6 < n < 8$	-8.16 ± 18.05	-13.98 ± 33.45	-31.04 ± 42.55
$0.15 < r_e(arcsec) < 0.3$	-0.94 ± 5.45	0.05 ± 13.79	-0.87 ± 32.27
$0.3 < r_e(arcsec) < 0.6$	-2.28 ± 9.02	-2.71 ± 20.11	-10.47 ± 35.21
$0.6 < r_e(arcsec) < 0.9$	-4.15 ± 12.67	-9.55 ± 24.26	-17.50 ± 40.12
$0.9 < r_e(arcsec) < 2.0$	-8.44 ± 18.68	-15.66 ± 32.69	-35.02 ± 43.53

$\delta n/n$	$20 < H_{AB} < 21.5$	$21.5 < H_{AB} < 23$	$23 < H_{AB} < 25$
$0 < n < 2$	-0.84 ± 6.23	-3.57 ± 16.86	-5.51 ± 39.42
$2 < n < 4$	-3.75 ± 8.71	-7.83 ± 20.63	-22.65 ± 39.74
$4 < n < 6$	-7.08 ± 12.33	-12.19 ± 24.38	-30.01 ± 39.47
$6 < n < 8$	-8.85 ± 14.25	-16.94 ± 26.32	-38.55 ± 36.30
$0.15 < r_e(arcsec) < 0.3$	-5.99 ± 12.04	-7.56 ± 22.54	-17.43 ± 39.18
$0.3 < r_e(arcsec) < 0.6$	-3.93 ± 10.03	-7.20 ± 21.14	-19.31 ± 38.89
$0.6 < r_e(arcsec) < 0.9$	-5.08 ± 11.05	-11.31 ± 21.56	-26.36 ± 39.79
$0.9 < r_e(arcsec) < 2.0$	-6.38 ± 12.51	-13.74 ± 25.47	-32.49 ± 41.78

Table 4. Relative errors (%) and standard deviations on the structural parameters depending on the apparent magnitude using five different PSFs (see Fig. 10).

	$0 < n < 2$	$2 < n < 4$	$4 < n < 6$	$6 < n < 8$
$20.0 < H_{AB,input}(mag) < 20.5$				
$\delta L/L$	-0.15 ± 2.95	-3.39 ± 5.48	-9.09 ± 7.90	-14.50 ± 8.47
$\delta r_e/r_e$	0.79 ± 5.25	-4.95 ± 9.28	-14.69 ± 14.79	-26.56 ± 16.21
$\delta n/n$	-4.39 ± 10.97	-13.84 ± 16.60	-24.76 ± 19.20	-36.22 ± 19.58
$20.5 < H_{AB,input}(mag) < 21.0$				
$\delta L/L$	-0.14 ± 3.82	-3.44 ± 6.32	-9.31 ± 9.39	-15.08 ± 9.23
$\delta r_e/r_e$	0.20 ± 5.36	-4.57 ± 10.89	-16.51 ± 16.28	-26.97 ± 17.87
$\delta n/n$	-4.16 ± 11.25	-13.82 ± 17.91	-23.84 ± 19.20	-38.19 ± 19.64
$21.0 < H_{AB,input}(mag) < 21.5$				
$\delta L/L$	-0.57 ± 4.92	-3.68 ± 7.55	-9.49 ± 9.25	-14.29 ± 10.06
$\delta r_e/r_e$	-0.86 ± 7.00	-5.73 ± 13.66	-16.66 ± 18.67	-26.05 ± 18.35
$\delta n/n$	-5.76 ± 12.02	-15.86 ± 17.54	-26.63 ± 20.50	-36.08 ± 19.52
$21.5 < H_{AB,input}(mag) < 22.0$				
$\delta L/L$	-0.49 ± 5.53	-4.59 ± 10.36	-9.94 ± 12.10	-14.68 ± 11.82
$\delta r_e/r_e$	-0.29 ± 7.33	-7.05 ± 17.72	-17.91 ± 22.02	-25.85 ± 24.09
$\delta n/n$	-6.04 ± 13.43	-16.61 ± 18.69	-27.84 ± 22.26	-36.30 ± 22.71
$22.0 < H_{AB,input}(mag) < 22.5$				
$\delta L/L$	-1.47 ± 7.60	-4.71 ± 13.41	-11.55 ± 13.82	-14.61 ± 15.32
$\delta r_e/r_e$	-1.75 ± 9.51	-7.38 ± 19.43	-16.97 ± 25.13	-26.68 ± 26.94
$\delta n/n$	-8.18 ± 17.99	-18.82 ± 21.73	-28.87 ± 22.24	-39.18 ± 24.90
$22.5 < H_{AB,input}(mag) < 23.0$				
$\delta L/L$	-1.67 ± 10.03	-5.89 ± 16.50	-11.89 ± 18.38	-17.96 ± 21.49
$\delta r_e/r_e$	-1.28 ± 11.40	-9.24 ± 26.02	-17.99 ± 29.22	-27.32 ± 34.57
$\delta n/n$	-8.25 ± 22.92	-18.29 ± 26.96	-29.25 ± 27.00	-41.66 ± 26.64
$23.0 < H_{AB,input}(mag) < 23.5$				
$\delta L/L$	-3.80 ± 19.13	-7.12 ± 22.24	-14.63 ± 19.75	-16.61 ± 24.12
$\delta r_e/r_e$	-2.84 ± 21.33	-10.78 ± 32.29	-20.79 ± 34.39	-25.78 ± 39.19
$\delta n/n$	-7.49 ± 29.62	-20.09 ± 33.28	-32.47 ± 31.11	-42.58 ± 29.90
$23.5 < H_{AB,input}(mag) < 24.0$				
$\delta L/L$	-1.89 ± 22.85	-10.19 ± 22.94	-14.19 ± 25.32	-20.52 ± 24.32
$\delta r_e/r_e$	-2.21 ± 27.87	-11.57 ± 35.12	-20.76 ± 39.58	-31.83 ± 41.51
$\delta n/n$	-3.87 ± 38.56	-24.95 ± 36.87	-36.53 ± 34.02	-46.46 ± 31.09
$24.0 < H_{AB,input}(mag) < 24.5$				
$\delta L/L$	-1.50 ± 25.40	-10.23 ± 32.27	-16.10 ± 34.15	-16.71 ± 36.33
$\delta r_e/r_e$	-3.60 ± 35.90	-14.78 ± 43.22	-30.37 ± 42.96	-30.21 ± 45.39
$\delta n/n$	-10.32 ± 42.23	-32.03 ± 42.13	-47.21 ± 38.40	-51.98 ± 36.24
$24.5 < H_{AB,input}(mag) < 25.0$				
$\delta L/L$	3.48 ± 38.67	-0.99 ± 47.79	-7.13 ± 48.32	-17.63 ± 39.12
$\delta r_e/r_e$	-11.83 ± 45.10	-24.02 ± 44.12	-33.58 ± 47.25	-36.64 ± 47.00
$\delta n/n$	-17.46 ± 48.50	-42.41 ± 46.73	-45.35 ± 44.40	-53.14 ± 39.50

Table 5. Relative errors (%) and standard deviations on the structural parameters using five different PSFs (see Fig. 11)

$\delta r_e/r_e$	$20 < H_{AB}(mag) < 21.5$	$21.5 < H_{AB}(mag) < 23$	$23 < H_{AB}(mag) < 25$
$0 < n < 2$	0.06 ± 5.77	-1.16 ± 9.59	-4.66 ± 32.39
$2 < n < 4$	-5.12 ± 11.07	-8.03 ± 21.95	-14.81 ± 38.86
$4 < n < 6$	-15.72 ± 16.22	-17.63 ± 25.57	-25.64 ± 41.12
$6 < n < 8$	-26.47 ± 17.73	-26.40 ± 29.20	-30.86 ± 43.40
$0.15 < r_e(arcsec) < 0.3$	-4.88 ± 13.91	-2.74 ± 16.53	-0.63 ± 31.95
$0.3 < r_e(arcsec) < 0.6$	-12.01 ± 15.03	-10.85 ± 19.95	-12.85 ± 34.54
$0.6 < r_e(arcsec) < 0.9$	-14.19 ± 17.17	-16.98 ± 24.64	-19.68 ± 40.32
$0.9 < r_e(arcsec) < 2.0$	-17.15 ± 21.19	-21.85 ± 30.48	-37.75 ± 43.51

$\delta n/n$	$20 < H_{AB} < 21.5$	$21.5 < H_{AB} < 23$	$23 < H_{AB} < 25$
$0 < n < 2$	-4.89 ± 11.68	-7.60 ± 18.65	-9.07 ± 39.19
$2 < n < 4$	-14.57 ± 17.28	-17.79 ± 22.82	-29.09 ± 40.43
$4 < n < 6$	-25.06 ± 19.75	-28.64 ± 23.92	-39.53 ± 37.22
$6 < n < 8$	-36.86 ± 19.70	-39.00 ± 24.87	-48.32 ± 34.49
$0.15 < r_e(arcsec) < 0.3$	-37.61 ± 22.17	-37.41 ± 24.34	-35.55 ± 39.30
$0.3 < r_e(arcsec) < 0.6$	-21.64 ± 20.35	-22.08 ± 24.19	-29.12 ± 39.11
$0.6 < r_e(arcsec) < 0.9$	-16.58 ± 18.55	-19.83 ± 23.63	-29.86 ± 40.01
$0.9 < r_e(arcsec) < 2.0$	-13.81 ± 17.93	-19.11 ± 25.80	-35.62 ± 42.06

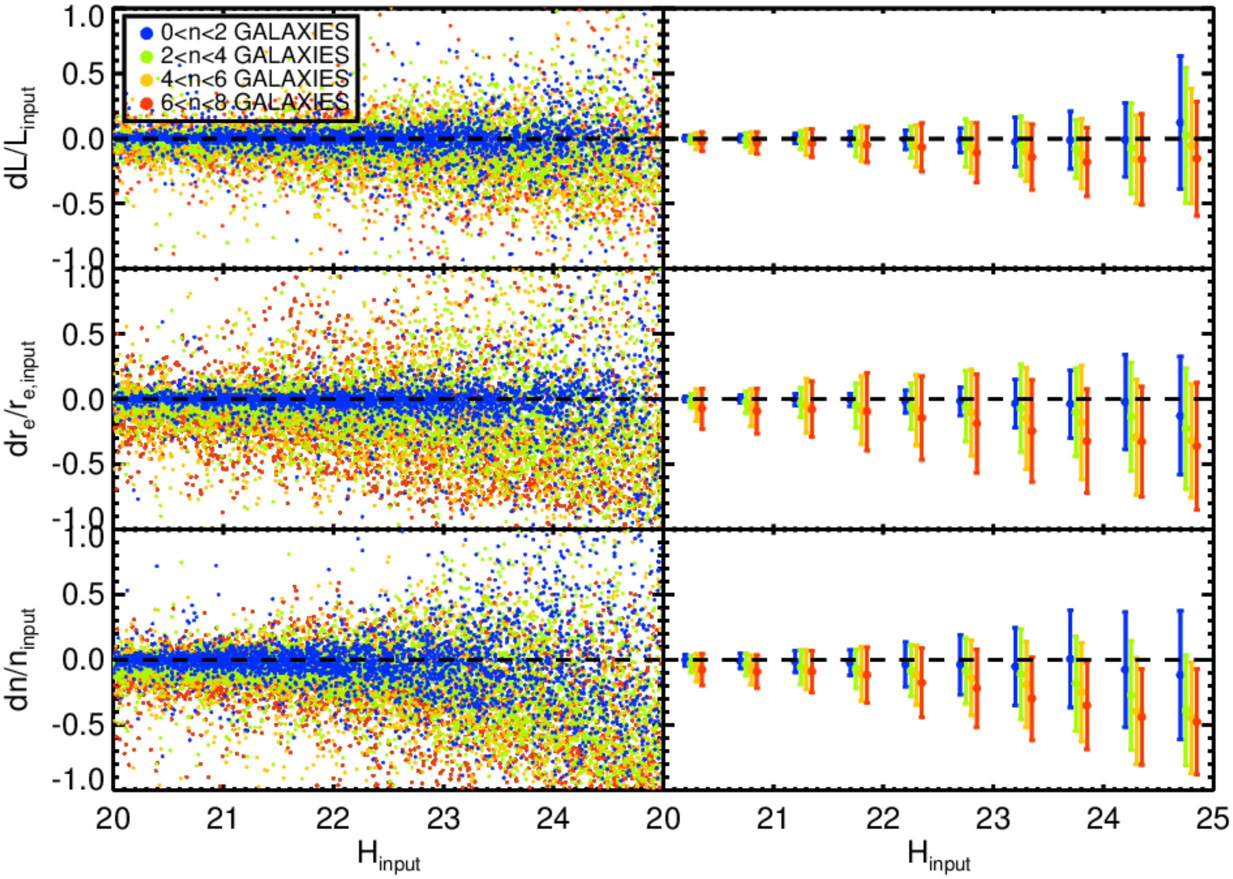

Figure 8. Relative errors - *(output-input)/input* - of the structural parameters (magnitude, effective radius and Sérsic index) of our simulated GNS galaxies. The right column shows the means in bins of 0.5 mag (with a 5σ outlier-resistant determination), being the error bars the standard deviation of the sample. The information in this plot is tabulated in Table 2.

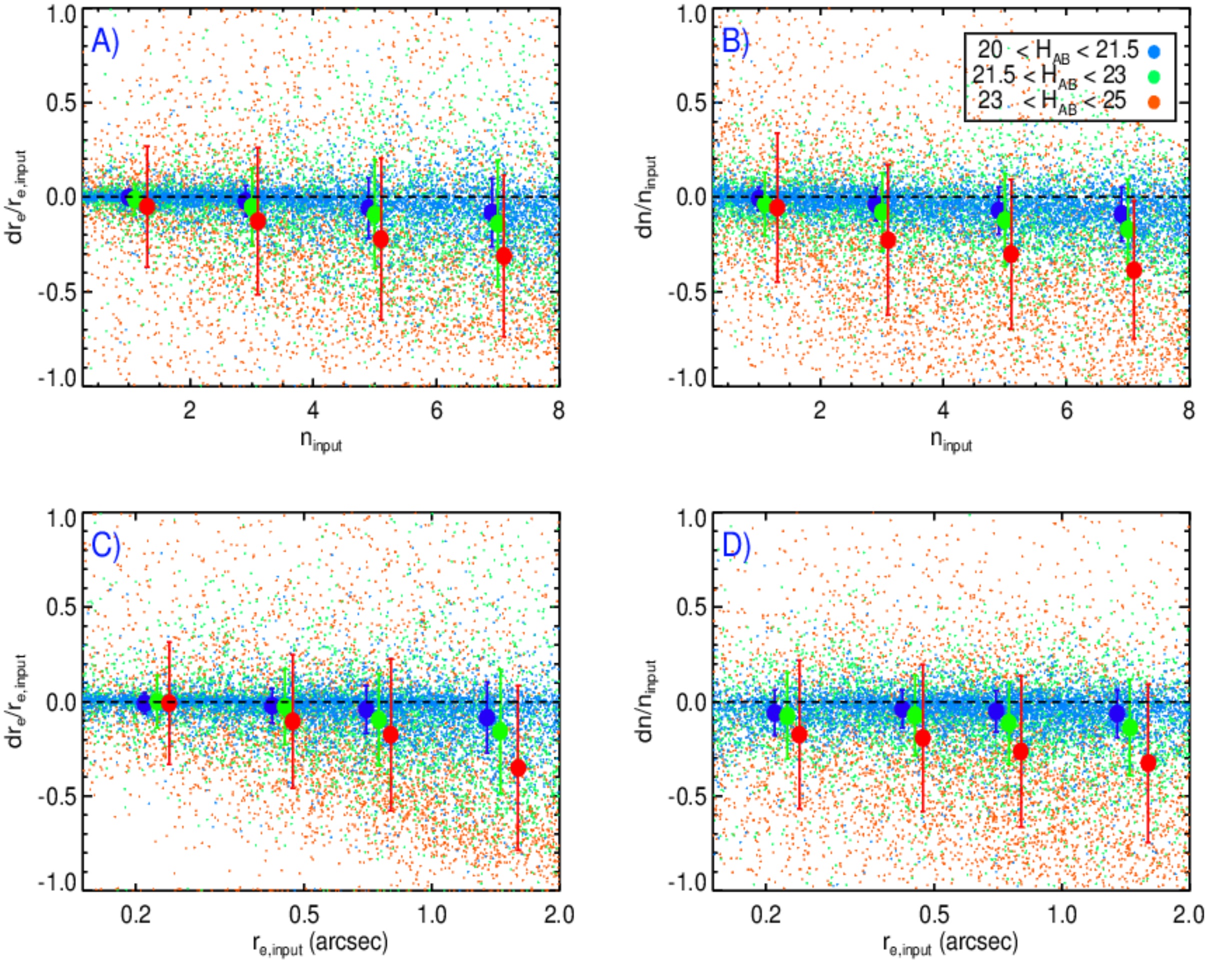

Figure 9. Relative errors - *output-input/input* - of the effective radius (first column) and the Sérsic index (second column) as a function of the input Sérsic index (first row) and the input effective radius (second row). Galaxies are coloured according to their magnitude. For the sake of clarity, mean values (derived with a 5σ outlier-resistant determination) where added using 4 intervals in effective radius and Sérsic index, with the error bars being their standard deviation. Sérsic index intervals are $0 < n < 2$, $2 < n < 4$, $4 < n < 6$ and $6 < n < 8$. Effective radius intervals are 0.15" $< r_e <$ 0.3", 0.3" $< r_e <$ 0.6", 0.6" $< r_e <$ 0.9" and 0.9" $< r_e <$ 2". Note that the colour of these mean points is the same as the one of the galaxy individual points. The information in this plot is tabulated in Table 3.

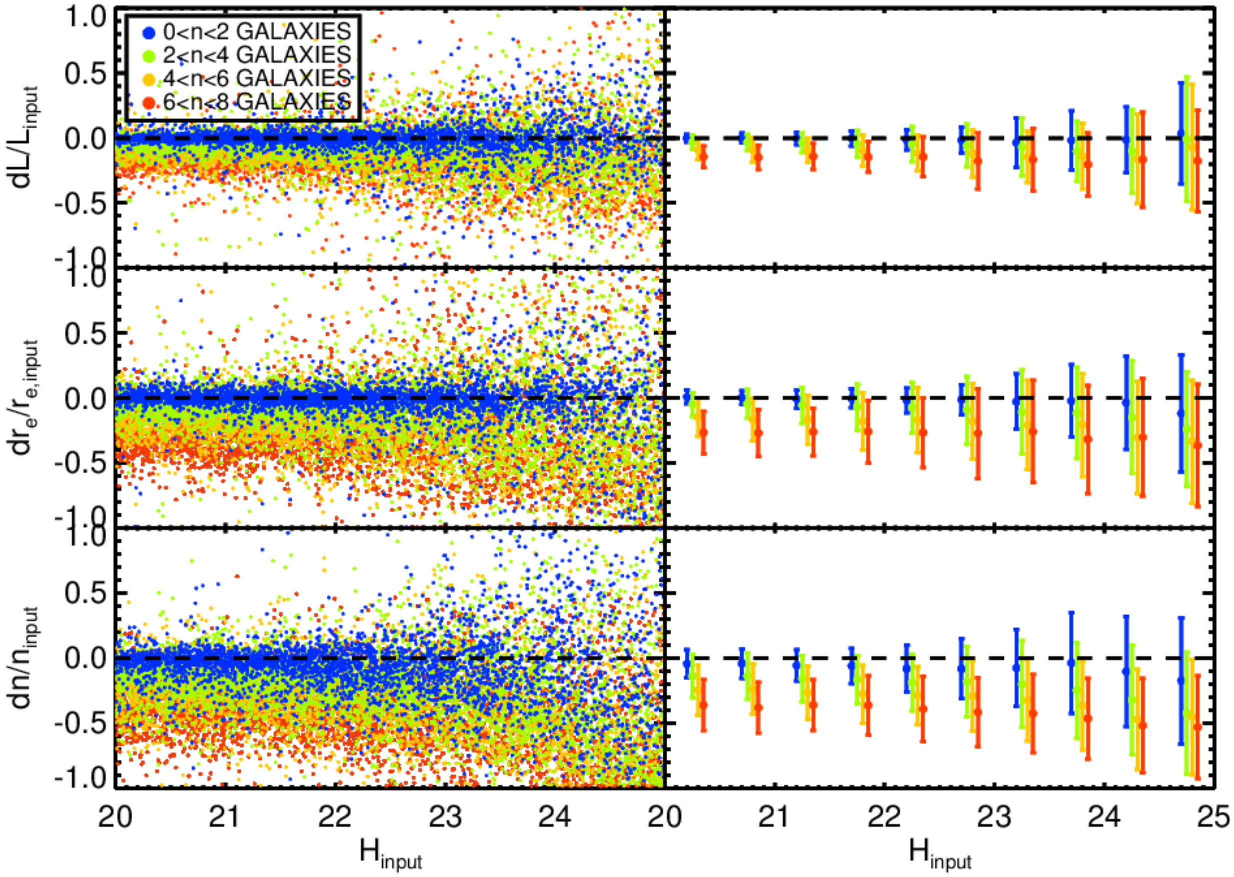

Figure 10. Same as in Figure 8, but using this time as the output parameters the mean values of the fits retrieved based on 5 different natural stars as PSFs. The results of this figure are tabulated in Table 4.

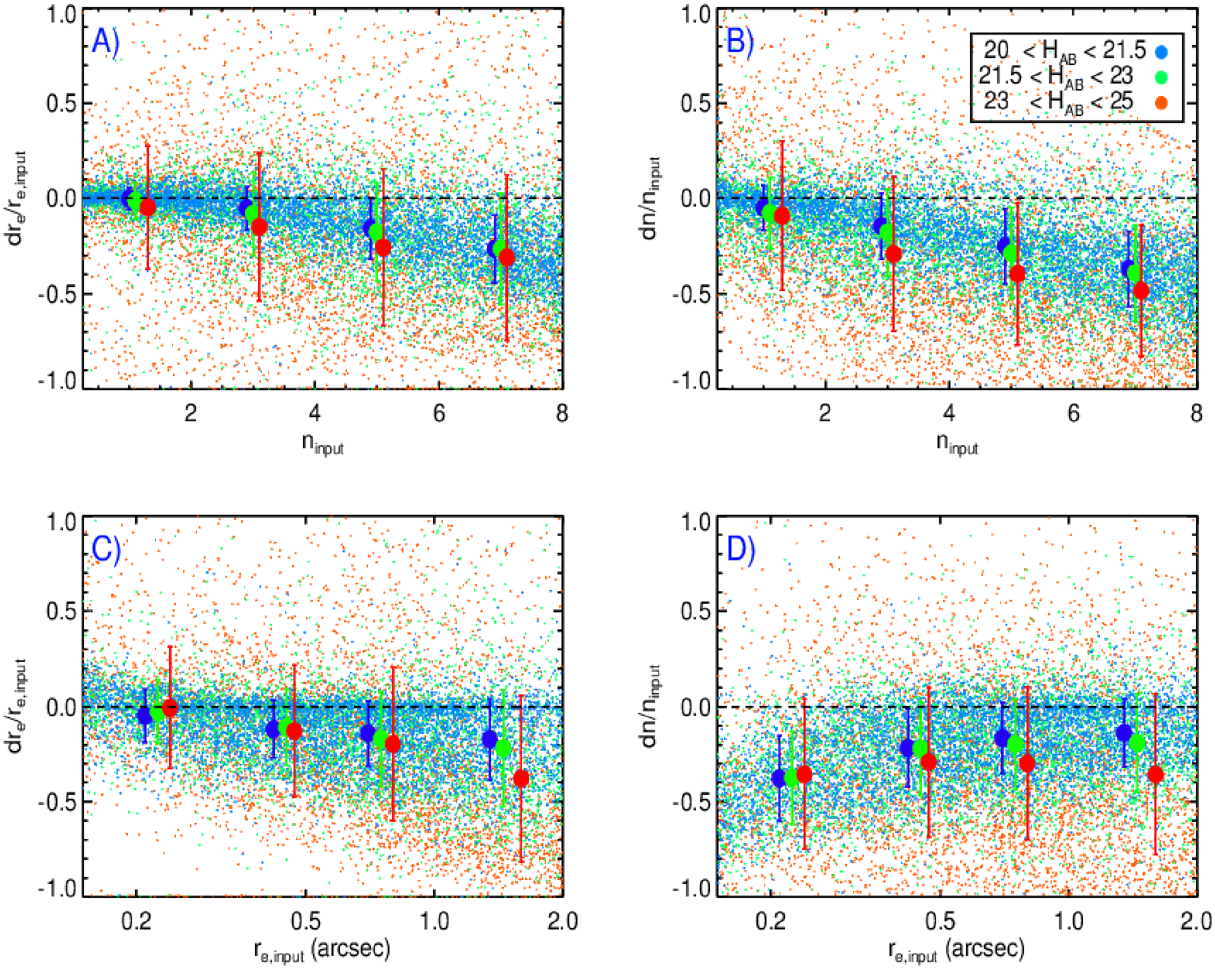

Figure 11. Same as Figure 9, but using this time as the output parameters the mean values of the fits retrieved based on 5 different natural stars as PSFs. The results of this figure are tabulated in Table 5.